8 Particle Physics with CMS at the LHC

Y. Allkofer, C. Amsler, V. Chiochia, A. Dorokhov, C. Hörmann, K. Prokofiev, H. Pruys, C. Regenfus, P. Robmann, J. Rochet, T. Speer, S. Steiner, and D. Tsirigkas[3]

in collaboration with:
ETH-Zürich, Paul Scherrer Institut (PSI) and the CMS Collaboration

(CMS Collaboration)

8.1 Physics programme

The Higgs boson mass is predicted to be smaller than 251 GeV (95 % C.L.) and LEP experiments have set a lower experimental limit of 114 GeV (95 % C.L.). A light Higgs decays mainly to $b\bar{b}$, a heavy Higgs mainly to four leptons via WW or Z^0Z^0 (Fig. 8.1). However, the two-gluon $gg \rightarrow b\bar{b}$ background dominates the signal for a light Higgs. For CMS one of the sensitive channels to search for a light Higgs is $H \rightarrow \gamma\gamma$ (Fig. 8.2). This is the motivation for the large electromagnetic calorimeter made of 80'000 $PbWO_4$ crystals.
The LHC is scheduled to start operations in 2007 at a center of mass energy of $\sqrt{s}$ = 14 TeV. The target luminosity is 10^{34} cm^{-2}s^{-1} which corresponds to an integrated luminosity of about 1 fb^{-1}, achieved every day, assuming full efficiency. This luminosity will hopefully be reached after 2 - 3 years of LHC operation. Figure 8.2 shows the required integrated luminosity for a 5σ Higgs discovery, as a function of mass. Since the final luminosity will not be obtained immediately, the Higgs is not likely to be observed during the commissioning years, unless it is rather heavy (see Fig. 8.2).
The Zurich group has therefore decided to concentrate first on issues related to B meson physics. At the LHC the cross section for $b\bar{b}$ production is five orders of magnitude higher than at the Tevatron and 10^4 $b\bar{b}$ pairs/s will be produced, even with a reduced luminosity of 10^{33} cm^{-2}s^{-1}. Also the physics involving B_s mesons ($\bar{d}s$ and $\bar{s}d$) will not be covered at the current B factories (since the $Y(4s)$ does not decay to $B_s\bar{B}_s$). For B physics the pixel detector we are constructing will be essential to tag secondary vertices from B decays.

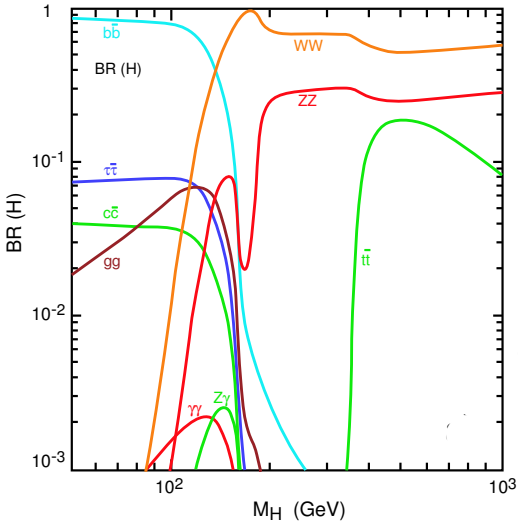

Figure 8.1:
Higgs decay branching ratios as a function of Higgs mass.

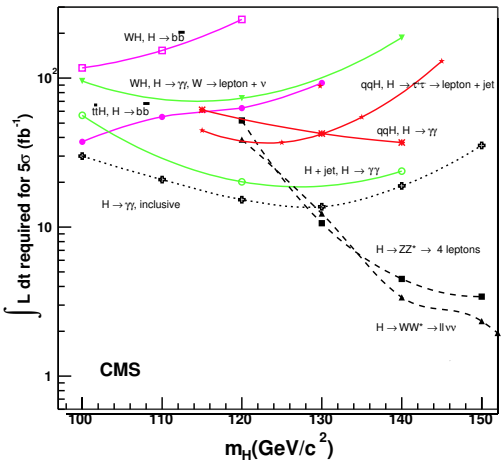

Figure 8.2:
Integrated luminosity required for a discovery with statistical significance of 5σ (1 fb^{-1} represents 1 day of LHC operation at full luminosity and efficiency).

[3]CERN doctoral student

We are preparing (1) a high statistics measurement of the decay channel $B_s \to J/\psi\ \phi$ with $J/\psi \to \mu^+\mu^-$ (or e^+e^-) and $\phi \to K^+K^-$. This channel is one of the golden channels to study many properties of B_s mesons such as CP violation in the B_s system and $B_s - \bar{B}_s$ oscillations. The search for rare B_s-decays such as $B_s \to \mu^+\mu^-$, $B_s \to \mu^+\mu^-\phi$, which have not been observed, opens windows for new physics beyond the standard model. Our experience with the reconstruction of B mesons at CMS will then be quite useful to search for the Higgs in a cleaner environment, such as the associated production $t\bar{t}H, H \to b\bar{b}$, leading to four jets containing b-quarks.

8.2 Performance tests of the silicon pixel detector

To reconstruct B mesons and suppress the dominating light quark and gluon background one has to determine the primary interaction and secondary B decay vertices. The optimum resolution is achieved with the first detector layer as close as possible to the beam-beam collision point. The first layer of our silicon pixel detector is at a distance of $\sim$ 4 cm from the interaction point. The very high particle flux near the primary vertex ($\sim$ 1000 particles every 25 ns) requires a highly granular detector composed of pixels delivering 3D coordinates with resolutions of the order of 15 μm.

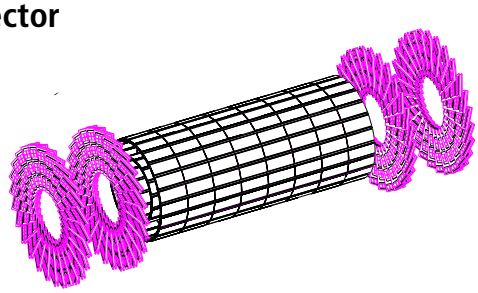

Figure 8.3:The CMS pixel vertex detector.

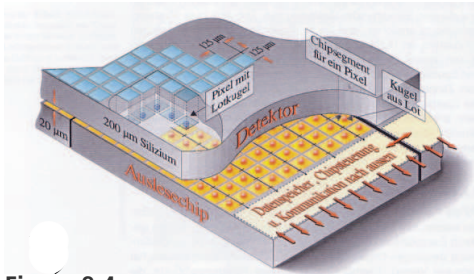

Figure 8.4:
Schematic view of a pixel detector element. Each sensor pixel is connected through an indium solder bump to a pixel unit cell on the readout chip which amplifies and processes the signal. The data are stored at the periphery of the chip where they wait for trigger confirmation.

The pixel detector consists of three concentric cylindrical layers, 53 cm long, with radii of 4.4, 7.3 and 10.2 cm and forward/backward wheels (Fig. 8.3). The latter wheels will be provided by the US collaborators while the barrel layers are built by the Swiss groups. The pixels are mounted on segmented sensor plates with readout chips in 0.25 μm technology, connected by indium bump bonds (Fig. 8.4). The analogue signals are read out to determine the coordinates more accurately, using charge sharing between pixels.

Radiation hardness is the main concern. We are using oxygen enriched silicon substrates which are more resistant to radiation. The pixels are formed by isolated n^+ implants and the pn junction is formed by a large p^+ implant on the backside (Fig. 8.5). The thickness of the sensor is 285 μm and the pixel size is 100 $\times$150 μm^2. The pixels must be separated by p^+ type isolation in order to prevent conductive interconnection between them caused by electron accumulation close to the surface between pixels. Two designs of p^+ dopants separations were tested, the p-spray design (Fig. 8.5, left) for which a moderate boron spray concentration has been diffused between pixels (produced by CiS, Erfurt), and the p–stop ring structure (Fig. 8.5, right) with very high boron concentration surrounding every pixel (manufactured by SINTEF, Oslo). To keep the pixel potential close to the readout chip potential (in the event of a pixel loosing the indium bump connection) the pixels are not completely isolated from each other. The high resistive inter–pixels connection is achieved by a punch–through structure and biasing grid in the the p–spray design and a gap in the p–rings for the p–stop design.

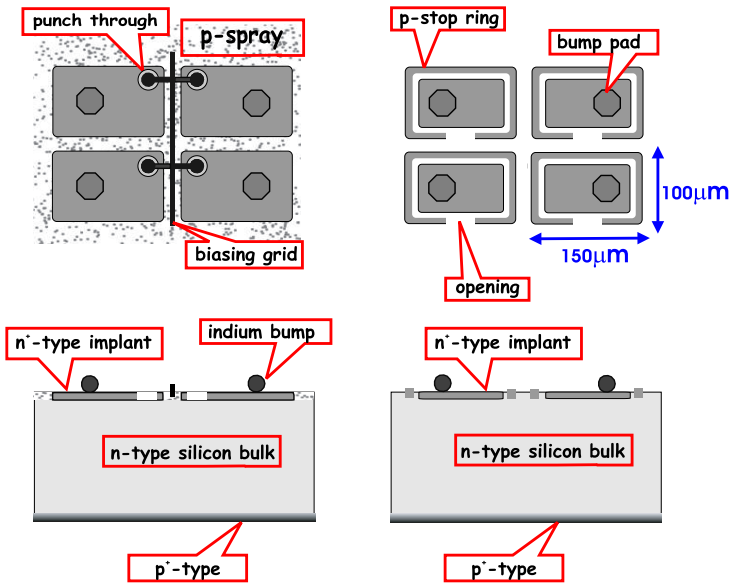

Figure 8.5:
Front view and cross section of the p-spray (left) and p-stop designs (right).

In 2004 we tested the performances of various pixel designs before and after irradiation. The pixel dimensions were of the former design (125 $\times$ 125 μm^2). They were irradiated up to a fluence of 10^{15} n$_{eq}$/cm^2 (neutron equivalent dose per unit surface) with 24 GeV protons from the CERN PS. For comparison the first four years of LHC operation gradually converging to the nominal luminosity correspond to 6 $\times$ 10^{14} n$_{eq}$/cm^2 for the innermost (4.4 cm) pixel layer.
The samples were tested with 150-225 GeV pions in the H2 beam line of the CERN SPS in 2003 and 2004 (2; 3). The beam test setup consisted of our beam telescope (4) made of 8 silicon microstrip detectors (4 measuring the horizontal x and 4 the vertical y impact points) with 50 μm readout pitch and a fast trigger diode. The pixel sensors were bump-bonded to an earlier readout chip (PSI30) and were mounted on a rotating support positioned between the second and third plane of the beam telescope (Fig. 8.6). The samples were stabilized at a temperature of -10 °C by means of water cooled Peltier elements. The hit coordinates on the sensor could be determined from the telescope with a resolution of $\sigma \sim 1$ μm. The telescope was inserted in the gap between two superconducting Helmholtz coils providing a field of 3 T (Fig. 8.7). Measurements were performed with the field parallel to the beam (to measure the Lorentz angle, see below) and perpendicular to the beam (to measure the position resolution).

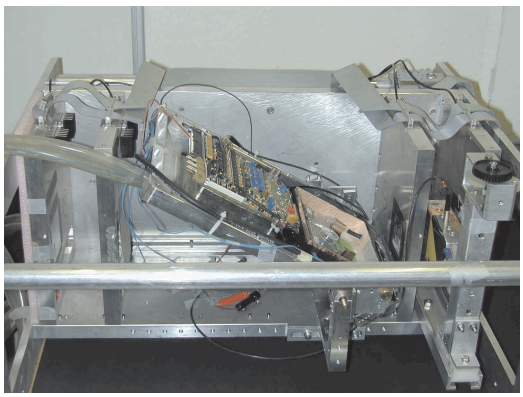

Figure 8.6:
Pixel sensor prototypes and readout inserted between the third and fourth plane of the silicon beam telescope.

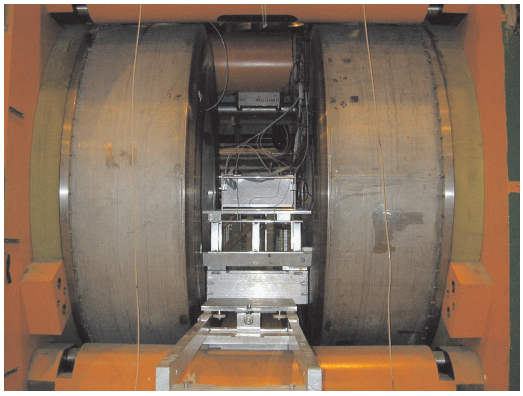

Figure 8.7: *Helmholtz coils providing a magnetic field of 3T.*

With our high resolution telescope it was possible to scan the surface of the sensors and to determine the charge collection efficiency. Irradiated sensors show trapping of charge carriers and the bias voltage has to be increased from typically 100 to 450 V to collect more charge and reach full depletion. Figure 8.8 shows the average charge collected for p-spray and p-stop before and after irradiation. The region with the highest collection efficiency is in the central part of the pixel corresponding to the n^+ implants. The charge collection efficiency is higher than for the p-stop design, about 60 % of that for unirradiated sensors after a fluence of 10^{15} n_{eq}/cm^2. The charge collection efficiency is lower in the punch-through regions in the case of the p-spray design. The p-spray and p-stop designs which were exposed to a fluence of 6×10^{14} n_{eq}/cm^2 have a particle detection efficiency of 99 % with a threshold of 2000 electrons. The respective value for the p-stop design is somewhat lower, 95 %. The p-spray design is therefore preferred over the p-stop.

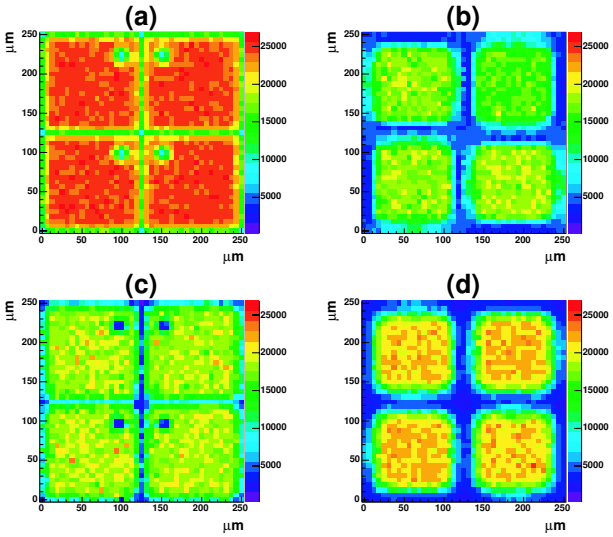

Figure 8.8:
Collected charge over the pixel surface at full depletion. Red (blue) corresponds to high (low) charge levels. The number of collected electrons is shown in the righthand bars. The plots on the left show the p-spray types before (a) and after irradiation with 6.7 $\times$ 10^{14} n_{eq}/cm^2 (b). The plots on the right show the corresponding charge for the p–stop designs.

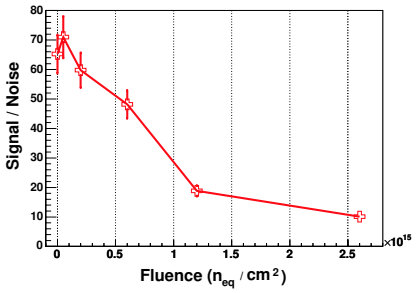

Figure 8.9:
Signal-to-noise ratio measured with the p-spray sensors as a function of irradiation.

The signal-to-noise ratio is about 70 for the unirradiated p-spray sensors, about 50 for the sensors exposed to a fluence of 6×10^{14} n_{eq}/cm^2, and about 10 for a fluence of 2.6×10^{15} n_{eq}/cm^2 (Fig. 8.9). Based on the results of these measurements (3) we have chosen the p–spray design for the barrel sensors. The results from the 2004 tests show that the pixel sensors can be operated up to irradiation fluences of 10^{15} n_{eq}/cm^2. This is much higher than what was originally specified for the CMS pixel detector.

8.3 Charge collection as a function of depth

The charge collection depends on the location of the charge deposit in the sensor bulk. The electron–hole pairs created in the bulk of a fully depleted unirradiated sensor reach the electrodes and contribute to the signal, while for irradiated sensors the trapping centers reduce the probability that charge reaches the electrode. This results in a smaller signal. The charge collection efficiency was measured with high energy pions crossing the sensor at a grazing angle α = 15° with respect to the pixel surface. The pixels at the distance x from the impact point along the beam direction sense the charge deposit at a depth $d = x \tan\alpha$ in the sensor.

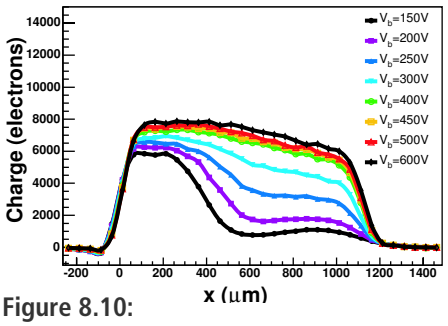

Figure 8.10:
Signal as a function of x for sensors exposed to a fluence of 6×10^{14} n_{eq}/cm^2 for various bias voltages.

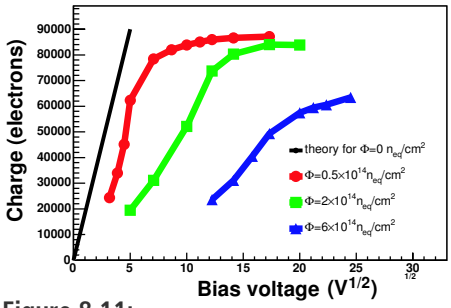

Figure 8.11:
Total collected charge as a function of the square root of the bias voltage far various fluences.

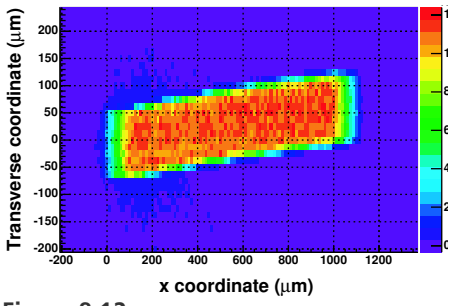

Figure 8.12:
Deflection of the charge in a 3 T magnetic field. The beam enters the sensors from the left.

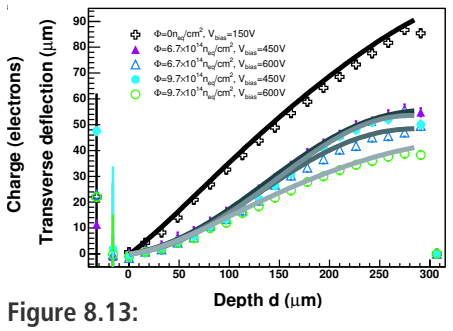

Figure 8.13:
Deflection at the surface versus depth at which the charge was produced, for various fluences.

Figure 8.10 shows the average signal as a function of x for various bias voltages and for a fluence of 6×10^{14} n_{eq}/cm^2. The depletion is believed to start from the implant side after irradiation leading to type inversion. Thus charge should be collected only from the depletion region close to the pixel implant at low bias voltages. However, the measured dependence of the charge collection efficiency (shoulder at high voltages) indicates that even at low bias voltages the charge is collected from both sides of the sensor. This means that for the irradiated sensors the depletion starts from both sides of the sensor bulk. In the conventional picture the total collected charge is proportional to $\sqrt{V_{bias}}$ up to full depletion voltage. The total charge collected is shown in Fig. 8.11 as a function of $\sqrt{V_{bias}}$. These curves do not exhibit the expected $\sqrt{V_{bias}}$ dependence, due the behavior of the electric field which does not vary linearly across the sensor depth, as expected for unirradiated devices. This observation is supported by the direct measurement of the electric field in the sensor bulk (3) and by a detailed simulation (5).

8.4 Lorentz angle as a function of depth

In the presence of a magnetic field the electrons and holes, are deflected from their drift along the electric field lines. We have measured the deflection angle (Lorentz angle θ_L) as a function of depth in the 3 T field provided by the Helmholtz coils of Fig. 8.7, using the technique described in ref. (6; 7). The beam enters the sensor plane at the grazing angle α and the magnetic field is parallel to the beam. Without magnetic field the charge generated at a given depth d would reach the pixel at a distance x along the beam line, as described in previous section. With magnetic field the charge is now deflected towards the adjacent pixel rows. Therefore, a measurement of the charge distribution among adjacent pixels yields the Lorentz angle θ_L as a function of x, and hence sensor depth (8).
Figure 8.12 shows the typical displacement of the collected charge at the surface of the sensor and Fig. 8.13 the displacement of the charge as a function of the depth at which the charge was produced, for various irradiation levels. One observes that the the displacement (and hence θ_L) decreases with irradiation. This is simply due to the increasing electric field needed to fully deplete the sensor. Extrapolating to 4 T one finds a Lorentz angle of $(26.3 \pm 0.8)^\circ$ close

to the pixel implants for the unirradiated sensor (100 V bias) and (11.6 $\pm$ 1.4)° after 6.7 $\times$ 10^{14} n_{eq}/cm^2 (450 V bias).
Figure 8.14 shows how θ_L depends on the sensor depth for various irradiation levels. The Lorentz angle appears to depend on depth. Since θ_L depends on E, B and the mobility (the latter also being a function of E), a measurement of θ_L as a function of depth determines the behaviour of the electric field as a function of depth. Using a well known empirical parameterization of the mobility one can extract the electric field as a function of sensor depth (3). Figure 8.15 shows that the electric field reaches maxima below both surfaces and a minimum in the bulk center.

8.5 Position resolution

The magnetic field was switched perpendicularly to the beam to reproduce the geometry of the CMS barrel sensors and the position resolution of irradiated sensors was measured with high energy pions in a magnetic field of 3 T (3). A simulation of the response of the 125 $\times$ 125 μm^2 was then performed, including the behaviour of the E-field described in the previous section, and verified with data. The simulation was then used to predict the expected charge sharing and the resolution for irradiated 100 $\times$ 150 μm^2 sensors of CMS at 4 T. Due to the widths of the (flat) modules the r.m.s resolution along the $r\phi$ direction (azimuthal angle direction) will vary with ϕ. It lies between 10 μm and 20 μm, depending on irradiation fluence and polar angle (Fig. 8.16). After the first four years of operation the resolution at the innermost barrel layer is still below 20 μm along the $r\phi$ direction and depends weakly on the polar angle. The resolution along the z direction is better than 20 μm. In conclusion, the pixel sensors for CMS will perform according to expectation and those at 4 cm from the collision point will fulfill the requirements at least during the first four years of LHC operation.

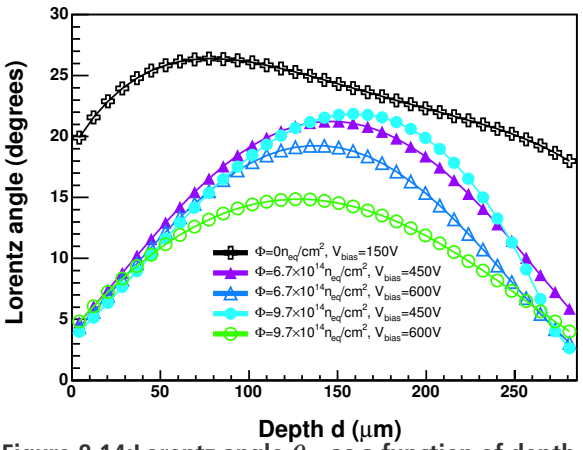

Figure 8.14:Lorentz angle θ_L as a function of depth.

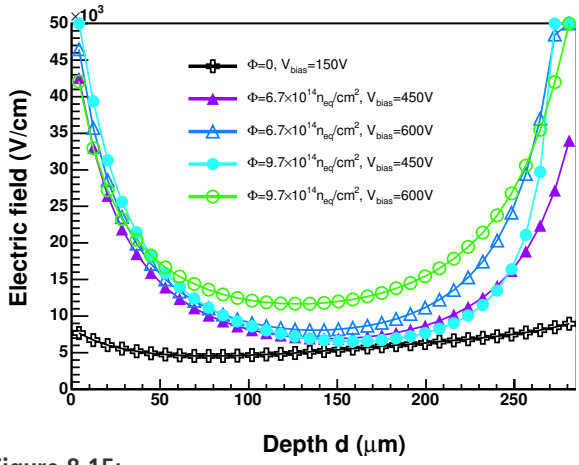

Figure 8.15:
Electric field as a function of depth. The regions immediately below the surfaces ($\sim$ 20μm) are affected by large systematic uncertainties.

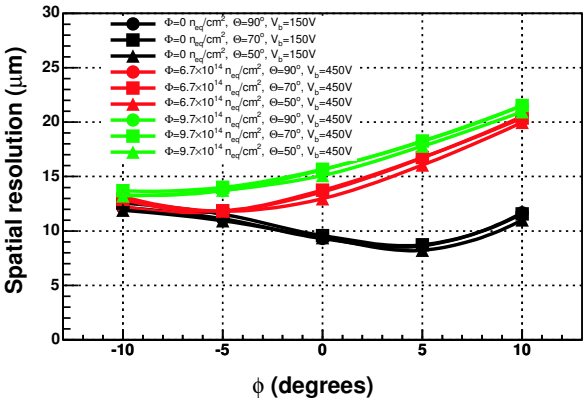

Figure 8.16:
Predicted $r\phi$ position resolution in the CMS pixel barrel as a function of azimuthal angle ϕ, for various polar angles θ and irradiation fluences.

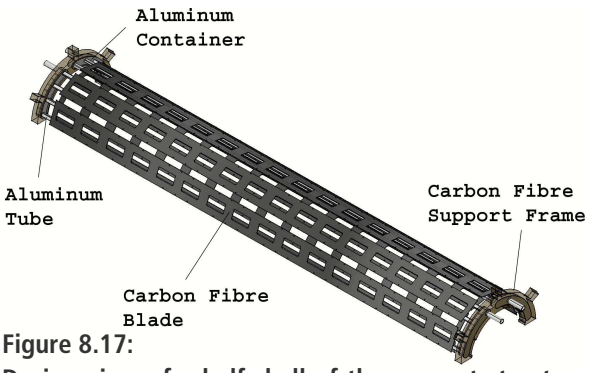

Figure 8.17:
Design view of a half shell of the support structure for the innermost pixel layer.

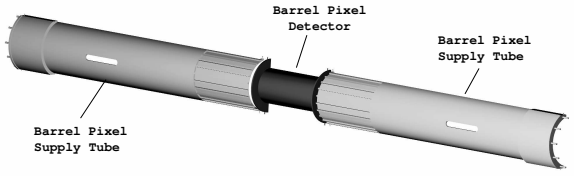

Figure 8.18:
Half shell of the barrel pixel detector system with its two service tubes.

8.6 Mechanical support structure

The design and construction of the mechanical support structure for the CMS pixel detector is performed by our group and our Institute's workshop. The detector support structures (Fig. 8.17) are made of aluminum tubes (wall thickness 300 μm) which are of trapezoidal shape to fit the geometrical constraints. The custom made 240 μm thick carbon fibre blades which support the pixel modules are then glued to the tubes forming the detector segments. Four to five of the aluminium tubes are laser-welded to an aluminum container which distributes the cooling fluid. Laser-welding is done in collaboration with industry. The manifold cools the detector modules to -20 °C using C_6F_{14} as a coolant. On both ends the manifolds are embedded in a carbon fibre support frame which supports the single segments and makes up the detector layer half shell.

We are also building the two 2.2 m long service tubes (Fig. 8.18) which transfer the power, all optical and electrical signals, and the cooling fluid to and from the detector. The power and slow control leads are embedded in the supply tube body. Foam will guarantee rigidity. The full system (pixel detector + service tube) is 5 m long. Two vertically separated half shells will be inserted into the CMS detector on a rail system. The insertion will be rather delicate since it will be done after the installation of the LHC beam pipe.

The design of the detector structure has been completed in 2004. The tools for the production of the different segment parts are also designed and manufactured. In 2005 we will continue with the leakage and cooling tests using the prototype segment of the support structure. Manufacturing of the final pixel segments and half shells will then start. Installation into CMS is foreseen during winter 2007/8, six months after LHC commissioning to avoid radiation damage during the initial injection trials.

8.7 Pixel power distribution

Our group is also responsible for the design of the CMS pixel detector power distribution for the front end electronics (low voltage) and the pixel sensors (high voltage) and cabling. The power lines are integrated in the service tubes discussed in the section above on mechanics.

In 2004 we have constructed a laboratory setup to mimic the behaviour of a section of the CMS pixel detector with respect to beam and settings induced voltage spikes. The system had to cope with sudden (100 ns) current excursions of 2 A in 50 m long power lines. Various solutions were tested to reduce the inductance of the cables. The setup includes a

prototype power supply unit housed in a VME-like crate, a mainframe unit controlling up to six crates, various power cables of the foreseen lengths, a prototype section of the service tube and active loads which reproduce the power consumption of the CMS pixel modules. The tests were performed to optimize the power supply units and the cable specifications to the pixel detector needs, i.e. to determine the need for additional electronics and grounding schemes. The development of the power supply unit is done in collaboration with CAEN, Viareggio, and preliminary results are encouraging.

8.8 Event reconstruction software

The Zurich group has adapted and implemented in the reconstruction software of CMS (ORCA) the Kalman filter (KF). This is a χ^2-square minimization which hence assumes that the track measuring errors are Gaussian distributed. Tracks are normally taken to be straight in the vertex neighborhood. We have improved on the KF by using more realistic helicoidal tracks in the homogeneous field of CMS. However, non-Gaussian noise (e.g. due to δ-electrons) is unavoidable. The distributions of the vertex pulls (difference between simulated and reconstructed values, divided by the measurement error) have a Gaussian core with tails.

We have shown that non-Gaussian noise can be taken into account with a Gaussian-Sum Filter (GSF) (9). Here the distributions of the measurement errors and the estimated quantities are modeled by linear superpositions (components) of Gaussian distributions. The main component describes the core of the distribution and the tails are described by one or several additional Gaussians. Several solutions for the vertex are then calculated with all combinations of components. The final vertex is calculated as the weighted average of all solutions. The algorithm was tested with a simplified simulation in which the tracks parameters were smeared with a mixture of two Gaussians. The hit positions, error estimates and χ^2 are significantly improved.

The sensitivity of the GSF with respect to badly measured tracks or tracks assigned to the wrong vertex (outliers) was extensively studied. These tests demonstrate a higher degree of robustness than χ^2-square estimators and show the adaptive power of the GSF for outliers for which higher weights are assigned to track-components with the largest standard deviations. A novel idea which emerged from these tests was the combination of the GSF with another non-linear filter, the *Adaptive Vertex Filter* (AVF) (10; 11). This filter is referred to as the *Adaptive-GSF* (A-GSF).

For example, an outlying track originating from a second vertex is added to the four tracks from the main vertex. The position of this vertex is shifted by between 0 and 5 mm in the transverse y direction relative to the jet-axis from the main vertex. The

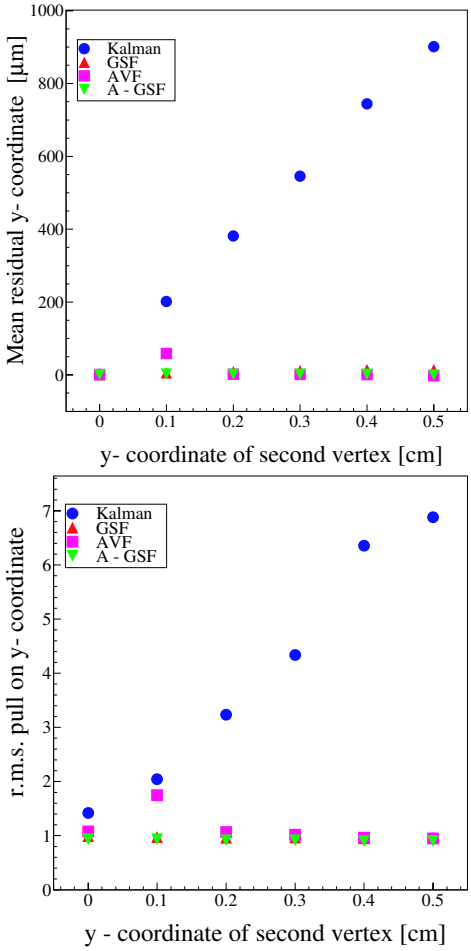

Figure 8.19:
Mean residuals (top) and standard deviations of the pull distributions (bottom) for different transverse positions of a vertex generated by an outlying track.

values of the mean residual distribution and the pull of the estimated vertex are shown in Fig. 8.19. The correct error assignments should lead to r.m.s. pulls of 1. The three non-linear filters are remarkably stable and improve substantially over the KF in terms of resolutions and pulls. For small displacements of the vertex, the AVF is not able to identify all of the outliers and is therefore slightly worse than the GSF and A-GSF. In particular situations the A-GSF performs much better than the GSF, but at the expense of a much longer CPU time.

In 2003/04 we also developed a kinematic fit based on Lagrange multipliers which incorporates additional constraints into the vertex fit to improve the resolutions. These constraints may be the masses of well known (long-lived) hadrons decaying to the observed particles, energy and/or momentum conservation, or collinearity in two-body processes. A further constraint of interest requires the momentum of the reconstructed B meson to be parallel to the vector pointing from the primary to the secondary vertex.

Considerable progress was made this year (1) . A framework for modeling the decay sequence is now provided. The fit allows for instance the reconstruction of complete decay chains, such as $B^- \to D^0 l^- \bar{\nu}_l$, followed by $D^0 \to K^-\pi^+$, $D^0 \to K^-\pi^+\pi^0$ or $D^0 \to K^-\pi^+\pi^-\pi^+$, where only the final long-lived particles are detected. The kinematic fit can also be performed with or without vertex constraint. The software is flexible enough so that new constraints can easily be included by the user.

One decay benefiting directly from such a kinematic fit is $B_s \to J/\psi\ \phi \to K^+K^-\mu^+\mu^-$, in which the Zurich group is particularly interested. This channel provides one of the best ways to determine the height η of the Unitarity Triangle. Here one measures the (CP violating) asymmetry between $B_s \to J/\psi\ \phi$ and $\bar{B}_s \to J/\psi\ \phi$. The CP-violating weak phase $\phi_{CKM} = [\arg(V_{cs}^* V_{cb}) - \arg(V_{ts}^* V_{tb})]$, measured in the rate asymmetry, is equal to $2\lambda^2\eta \simeq 0.03$, where λ is the sine of the Cabibbo angle. A measurement of a significantly larger phase ϕ_{CKM} would indicate contributions from non-Standard Model processes. These parameters may be obtained by a classical maximum-likelihood analysis or by an angular correlation analysis.

Our group is involved in the analysis of this decay with simulated data to estimate the sensitivity of the CMS detector. We have devised a selection strategy that relies on the partial reconstruction of the four charged tracks, already at the stage of the high level trigger (HLT). Indeed, by restricting the track reconstruction to the first 5 hits (to save CPU time) the precision on the track parameters is already sufficient. At the first level the dimuon trigger selects two muons of opposite charges with a transverse momentum above 3 GeV/c, using only the measurements from the muon chambers.

In the HLT the muons stubs are projected into the tracker and all tracks in a cone around a muon candidate are reconstructed. We require the presence of two muons tracks of opposite charges with an invariant mass within 100 MeV of the mass of the J/ψ, as well as two kaon tracks of opposite charges with an invariant mass within 100 MeV of the ϕ mass. The four tracks are required to come from a common secondary vertex by imposing a requirement on the confidence level of the vertex fit. As CMS lacks particle identification (with the exception of muons) all charged tracks have to be considered as possible kaon candidates. This adds a significant contribution to the background from combinatorial ambiguities.

The kinematic fit is applied during offline reconstruction. The r.m.s. resolution in the invariant mass is 14 MeV and the corresponding resolution σ_{ct} on the mean decay path $c\tau$ = 438 μs in the B_s rest frame is 35 μm (Fig. 8.20). A preliminary study shows that approximately 125'000 fully reconstructed B_s candidates will be obtained in the first year of LHC operation at the reduced luminosity of $2 \times 10^{33}\mathrm{cm}^{-2}\mathrm{s}^{-1}$.

We are also investigating the analogous decay $B_s \to J/\psi\,\phi$ where $J/\psi \to e^+e^-$. This decay will increase the B_s sample but the reconstruction of low-momentum electrons is notoriously difficult. All these studies will be incorporated into the physics technical design report requested by CERN in summer 2005.

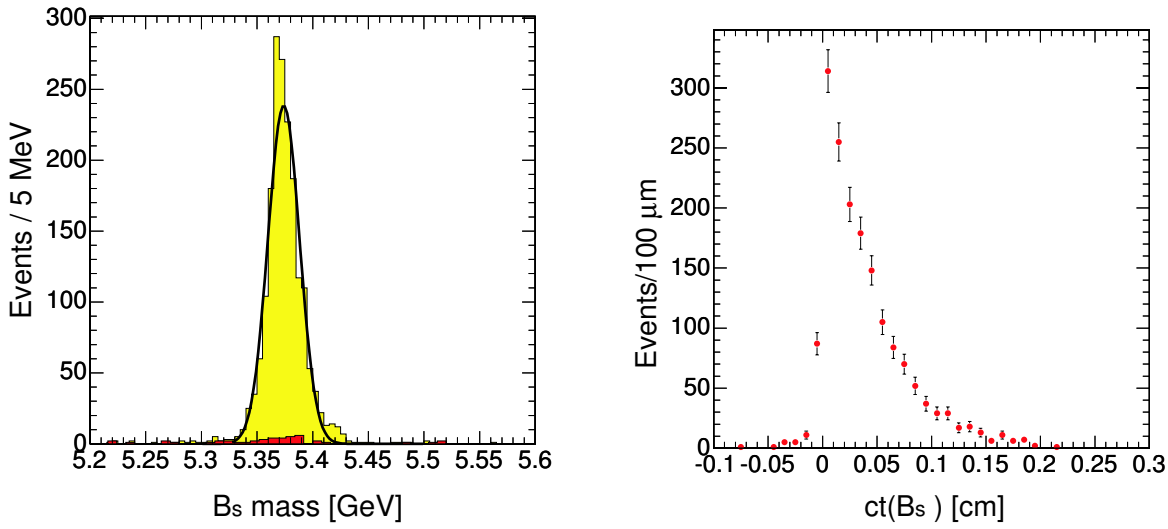

Figure 8.20:
Left: Invariant mass distribution of $B_s \to J/\psi\,\phi$ candidates after the kinematics fit. The small red area is the residual combinatorial background.
Right: ct distribution.

[1] K. Prokofiev, PhD thesis, in preparation.
[2] A. Dorokhov *et al.*, Nucl. Instr. and Meth. in Phys. Research A **530** (2004) 71.
[3] A. Dorokhov, PhD thesis, Universität Zürich, 2005.
[4] C. Amsler *et al.*, Nucl. Instr. and Meth. in Phys. Research A **480** (2002) 501.
[5] V. Chiochia *et al.*, Proc. 2004 IEEE Nuclear Science Symp., prep. physics/0411143.
[6] R. Kaufmann, PhD thesis, Universität Zürich, 2001.
[7] B. Henrich and R. Kaufmann, Nucl. Instr. and Meth. in Phys. Research A **477** (2002) 304.
[8] A. Dorokhov *et al.*, Proc. Vertex 2004 Conf., prep. physics/0412036.
[9] R. Frühwirth and T. Speer, Nucl. Instr. and Meth. in Phys. Research A **534** (2004) 217.
[10] R. Frühwirth, K. Prokofiev, T. Speer, P. Vanlaer and W. Waltenberger, Nucl. Instr. Meth. in Phys. Research **A 502** (2003) 699.
[11] J. D'Hondt, P. Vanlaer, R. Frühwirth and W. Waltenberger, IEEE Trans. Nucl. Sci. **51** (2004) 2037.